Experimental multiple parameters optimization of the injection strategies for a turbocharged direct injection hydrogen engine to achieve highly efficient and clean performance

Shi-wei Zhang [a], Bai-gang Sun [a, b], Qing-he Luo [a, b], Ling-zhi Bao [a,c *], Xiang-yu Li [a], Felix Leach[c]

a School of Mechanical Engineering, Beijing Institute of Technology, Beijing 100081, China

b Beijing Institute of Technology Chongqing Innovation Center, Chongqing, 401121, China

c Department of Engineering Science, University of the Oxford, Oxford, OX1 3PJ, UK

Corresponding: Ling-zhi Bao (Email: paul.bao@eng.ox.ac.uk)

Abstract

Improving the brake thermal efficiency (BTE) and reducing NOx emissions are two main goals for hydrogen-powered internal combustion engines to achieve efficient and clean performance. This paper focuses on the multiple parameters optimization of injection and ignition both experimentally and numerically based on a 2.0L turbocharged direct injection hydrogen engine. Firstly, the effects of single and split injection on engine performance, in-cylinder mixing and combustion characteristics are investigated. Secondly, the single-factor effect of split injection parameters and spark timing on engine performance are obtained with different engine speeds. Significant interaction effects are detected between these factors. Thus, a multi-parameter optimization is conducted based on the response surface methodology method to analyze the co-relationship of factors (split injection control parameters and ignition) on responses (BTE, NOx

emissions, and knock intensity) at high-load. Finally, a maximum BTE of 43.03% and a reduction in NOx emissions by 71.19% are achieved with the help of model prediction at 2500 rpm and a load of 1.40MPa. Further optimization of other engine speeds is conducted, and the boundary of high-efficiency region (BTE>40%) covers over 50% of the load map after optimization. These results can provide valuable support for the performance improvement of efficiency and clean hydrogen engines.

Keywords: Hydrogen engine, Direct injection, High thermal efficiency, Injection optimization, Multiple Injection

Nomenclature

H_2ICE	Hydrogen internal combustion engines
PEMFC	Proton exchange membrane fuel cells
DI	Direct injection
PFI	Port fuel injection
VGT	Variable geometry turbocharger
WGT	Waste gate turbocharger
VVT	Variable valve timing
IVO	Intake valve opening
SOI	Start of injection timing
EOI	End of injection timing
SSOI	Secondary start of injection timing
SEOI	Secondary end of injection timing
SIMP	Secondary injection mass proportion
MAP	Manifold air pressure
λ	Excess air coefficient
BMEP	Brake mean effective pressure
IMEP	Indicated mean effective pressure
BTE	Brake thermal efficiency
BP	Brake power
MBT	Minimum spark advance for best torque
ICEs	Internal combustion engine vehicles
MAPO	Maximum amplitude pressure oscillation
TKE	Turbulent kinetic energy
RSM	Response surface methodology

CCD	Central composite design
ANOVA	Analysis of variance

1. Introduction

Climate change and energy security are among the most pressing challenges confronting the global community. The International Energy Agency (IEA) ranks the transportation sector as the second-largest contributor to global carbon emissions, responsible for about 16% of the total, and the decarbonization of the transportation industry has emerged as an inescapable trajectory [1]. Within the context of contemporary global economic and political strategies, hydrogen is increasingly recognized as a viable and prospective zero-carbon energy carrier [2].

Hydrogen, as a clean and efficient alternative fuel, holds significant potential for internal combustion engines (ICEs) [3]. The unique properties of hydrogen, such as its high diffusion coefficient and wide flammability range, present both opportunities and challenges in optimizing engines, including injection strategies and mixture formation [4]. Direct injection of hydrogen can facilitate stratified combustion, where optimal stratification accelerates flame propagation, enhancing the stability of a lean combustion regime. This approach effectively mitigates knock and diminishes heat transfer losses through the cylinder wall [5].

The performance and emissions of direct injection hydrogen internal combustion engine (DI-H_2ICE) have made significant process with the help of turbocharging, exhaust gas recirculation (EGR), and water injection technologies [6,7]. Lai et al. [8] investigated the boundary matching and optimization strategy of a variable geometry turbocharged DI-H_2ICE, and achieved a maximum BTE of 42.53% and peak power of 124.8 kW. Bao et al. [9] optimized the control strategy of the turbocharged DI-H_2ICE to achieve near-zero emissions at a high power of 73 kW and brake thermal efficiency (BTE) of 41.2 %. In addition, EGR was

demonstrated to increase brake power (BP) and decrease emissions [10]. Koch et al. [11] showed that using EGR to avoid knock in a hydrogen-fueled engine, the BP can be increased from 150 to 180 kW. Kawamura et al. [12] demonstrated an optimized EGR rate of 30%, resulting in a reduction of NOx of about 50% while maintaining a high indicated thermal efficiency (ITE) of 45% in a 1.054L hydrogen engine.

Apart from the above method, the engine performance and NOx emissions have been proven to be sensitive to hydrogen injection strategy. Both injection timing and injection pressure affect the distribution of mixing gas which is closely related to the combustion quality and NOx emissions. The injection timing optimization is widely investigated by researchers based on the engine test. Bao et al. [13] and Zhao et al. [14] demonstrated that before optimizing injection timing, the engine's BTE is 40.4% at a load of 0.88 MPa with an SOI (Start of Injection) at -180°CA (negative values represent crank angles before TDC). Additionally, the BTE increases to 41.7% when the SOI is retarded to -80°CA. However, the NOx emissions rise rapidly to 317 ppm. After optimizing the EOI (End of Injection) to -80°CA, the BTE increases to 41.4% at a load of 1.0 MPa, with NOx emissions reduce to below 20 ppm. Wei et al. [15] showed that when injection timing is delayed, heat losses are reduced and BTE is improved. However, late injection timing causes an obvious increase in NOx emissions. On the other hand, Mohammadi et al. [16] demonstrated that retarding the hydrogen injection timing during the compression stroke can increase the BTE more than 38.90%. Moreover, late injection of hydrogen leads to a significant reduction in NOx emissions, primarily due to lean combustion conditions at high engine loads. Huang et al. [17] proposed that the homogeneity of the mixture distribution becomes worse with the delay of the start of injection (SOI), because a rich mixture was distributed near the cylinder wall, resulting in a decrease of BTE. Lee et al. [18] investigated three mixture formation modes: homogeneous charge, lean-homogeneous charge, and lean-stratified charge under three different injection

timing. Their results showed that lean-stratified charge mode had the highest ITE of 34.09 %. Moreover, Ye et al. [19] found that the uniformity of mixture increases with the advance of injection timing and the intensity of knock initially decreases and then increases with the delay of injection timing. Early injection can promote the in-cylinder swirl in a clockwise direction with their engine design. The flame propagation distance of the anticlockwise direction is longer than the clockwise one and the flame speeds increases with the advance of injection timing.

Injection pressure is also another important parameter to be considered in injection strategy. Huang et al. [17] explored the impact of two hydrogen injection pressures (5 MPa and 10 MPa) and timing on mixture formation and combustion characteristics. They showed that low injection pressure with stratified combustion can achieve good performance. Moreover, Kawamura et al. [12] compared the NOx emissions with injection pressure between 10 MPa and 20 MPa in a 1.05 L multi-cylinder hydrogen engine with two types injectors. The first injector was needle valve type, driven by working fluid with the maximum injection rate of 90 mL at 20 MPa. While the secondary injector was plate valve type, driven by an electric magnet with the maximum injection rate of 180 mL at 10 MPa. It was found that 20 MPa is less advantageous than 10 MPa. In addition, Hu et al. [20] compared high injection pressure (15 MPa) and low injection pressure (2 MPa) based on a 3-cylinder turbocharged DI H_2ICE. The results indicated that low-pressure injection exhibits superior combustion performance compared to high-pressure injection under retarded SOI = -120 °CA. However, the study emphasized that the need to increase the nozzle diameter to compensate for reduced flow rates at low-pressure (2 MPa).

Apart from single injection, split injection is also regarded as an important injection strategy which can lead to a stratified mixture, respectively forming a local rich area and lean area, and avoiding the air-fuel ratio

region with high NOx emissions in the cylinder [21–24]. A high-pressure hydrogen injection of 10 MPa was applied and optimal multiple injection strategies have the potential to reduce NOx emissions by up to 85 % compared to single injection while maintaining constant engine ITE of 30% by Wallner et al. [25]. However, due to the limitation of injector time response, multiple injection strategies are constrained at high engine speeds. Besides small quantities of multiple hydrogen Injections will not break the air boundary layer of the chamber walls, and low cooling loss with high thermal efficiency is expected according to Yamane et al. [26]. Welch et al. [27] founded that multiple injections can offer nearly an order of magnitude NOx reduction with a slight penalty in efficiency versus single injection (NOx=2600 ppm with single injection, NOx=400 ppm with multi-injection) when λ exceeds 1.67 at 1500 rpm. Liang et al. [28] investigated the effects of single and split injection strategies on combustion and emissions, revealing that early hydrogen injection leads to pre-ignition (as previous studies have found). The use of split injection strategies was shown to impact the in-cylinder pressure and heat release rate (HRR). The study highlighted the importance of adjusting the second injection timing and proportion to balance efficiency and NOx emissions also addressed by Li et al [29], who found that delaying the SOI improved the combustion process and thermal efficiency under certain conditions. However, they also noted that increasing the SIMF to more than 30% could lead to a significant increase in NOx emissions, highlighting the need for a balance between performance and emissions.

By reviewing study related to injection strategies of DI-H_2ICEs, it is found that optimized injection parameter is crucial for enhancing thermal efficiency and reducing NOx emissions. Split Injection can flexibly control the formation mixing gases for the whole operating conditions, providing higher combustion quality while keeping low NOx emissions. Prior research has achieved some basic injection optimization results by experiments but mainly focuses on low engine speeds below 2000 rpm with medium engine loads.

However, large injection mass and short injection duration windows at high load and high speed require further adjustment of proper injection strategy. Additionally, previous studies mainly focused on the single-factor effects of injection parameters, the synergistic effects between injection timing, injection pressure and ignition may ignore. To ensure a more comprehensive exploration of multi-parameter combinations, response surface methodology (RSM) is applied to simultaneously optimize split injection parameters and ignition timing. In this study, experimental and numerical analysis are used based on a 2.0 L turbocharged H_2ICE to propose suitable injection strategies. A fast-response DI hydrogen injector is used and the optimal split injection is tested under the whole speed range from 1000 rpm to 4500 rpm to achieve higher BTE and low NOx emissions with a BMEP of over 1.2 MPa. Significant interaction effects are detected between the engine performance and injection strategy. The result and optimizing process is valuable to develop highly efficient and clean DI- H2ICE.

2. Experimental and Numerical methods

2.1.Test rig

The engine specifications are listed in Table 1, and the schematic diagram of the test rig is shown in Fig. 1.

Table 1 Engine specifications

Parameters	Values
Engine type	4-cylinder, 4-stroke
Bore	80.5 mm
Stroke	98 mm
Displacement	2.0 L
Number of valves	4
Compression ratio	12.5
Turbocharging	Variable geometry turbocharger

Hydrogen injection pressure	6~12 MPa

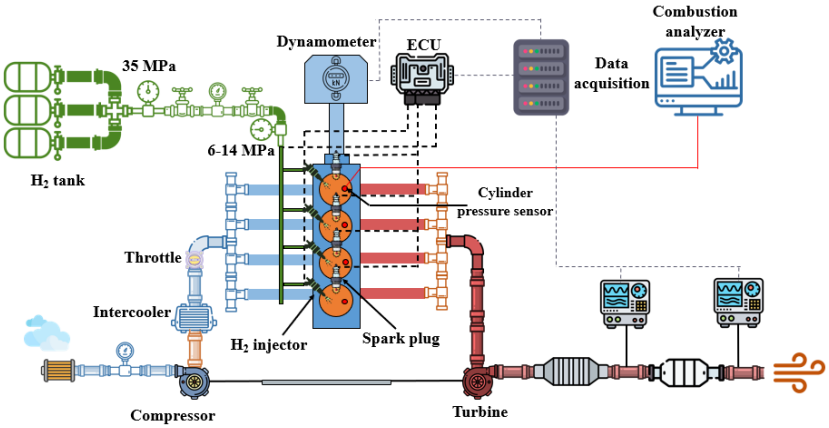


Fig. 1 Schematic diagram of the test rig

Fast-response Bosch HDEV6 hydrogen injectors are side-mounted in each cylinder, which operates by electromagnetic solenoid control. It differs from its predecessor, the HDEV4 injector which is driven by a piezoelectric crystal. Thus, the need for a 240 V boost voltage is eliminated and the size of the ECU controller is reduced. Moreover, HDEV6 hydrogen injector has been demonstrated to achieve high flow rates and is capable of operating at low pressures. Specifically, the HDEV6 injector reaches a hydrogen flow rate of 4.36 mg/ms at an injection pressure of 12 MPa, marking a substantial (63.90%) increase over the 2.66 mg/ms achieved by the HDEV4 injector at 14 MPa injection pressure. The enhanced hydrogen flow and precise electromagnetic control facilitate the development of injection strategies, enabling the adoption of split or multiple injections.

As illustrated in Table 2, the engine speed and torque are measured by a CW250 eddy current dynamometer. A two-stage pressure-reducing valve is employed to regulate the hydrogen injection pressure, allowing adjustment from 4 MPa to 20 MPa as per the testing requirements. Cylinder pressure measurements are conducted using four Kistler cylinder pressure sensors (Kistler 6052C), and the electric control unit (ECU) is implemented using an INCA system. Additionally, temperature readings are obtained by PT100 sensors

and K type thermocouples, and the intake and exhaust manifold instant pressures are integrated into the data acquisition system.

Table 2 Measuring equipment parameters

Equipment	Device	Accuracy
Dynamometer	GW250	Torque: ±0.1 N m/Speed: ±1 rpm
Pressure sensor	Kistler 6052C transducer	±0.02 MPa
Air mass flow meter	MTR-500 Air flowmeters	±1% Full Scale
Hydrogen mass flow meter	CMF010 H_2 flowmeters	±0.01 kg/h
Exhaust gas analyzer	AVL Di-TEST GAS 1000	±3 ppm for NOx

The mass flow of hydrogen was monitored using Emerson CMF010 Coriolis mass flowmeters with high accuracy (±0.01 kg/h), and a thermal mass flowmeter was used to measure the mass flow of air. The excess air coefficient (λ), calculated for each operating condition as the reciprocal of the equivalence ratio, was determined based on the measured mass flow rates of hydrogen and air within the test bench system. NOx emissions in the exhaust gases were measured using an AVL Di-TEST GAS 1000 which uses the electrochemical method.

The indicated thermal efficiency (ITE) is calculated by Eq.(1)

$$\text{ITE}\ (\%) = P_i / \left(\dot{M}_{H2} * H_u\right) \tag{1}$$

Here, $\dot{M}_{H2}$ is the hydrogen mass flow and H_u is the lower heating value of hydrogen. P_i is the indicated power calculated from the indicated mean effective pressure (IMEP), which is derived from the cylinder pressure trace by:

$$\text{IMEP} * V_h = \oint p * \mathrm{d}V \tag{2}$$

The brake thermal efficiency (BTE) can evaluate the efficiency of engine operation. P_e is the effective work tested by the dynamometer and the BTE is calculated by Eq.(3)

$$\text{BTE}\ (\%) = P_e / \left(\dot{M}_{H2} * H_u\right) \tag{3}$$

The coolant energy proportion indicates the energy absorbed by the coolant and the coolant energy proportion is calculated by Eq.(4)

$$\text{Coolant energy proportion}\ (\%) = \dot{M}_{\text{Coolant}}\, c_{\text{p,Coolant}}(T_{\text{Coolant,out}} - T_{\text{Coolant,in}})/(\dot{M}_{H2} * H_u) \quad (4)$$

Here $\dot{M}_{\text{Coolant}}$ represents the mass flow of the coolant; $c_{\text{p,Coolant}}$ represents the specific heat capacity of the coolant; $T_{\text{Coolant,out}}$ and $T_{\text{Coolant,in}}$ represent the temperature of the coolant entering and exiting the engine, respectively.

2.2 Test arrangements

As shown in Table 3, during the test, the injection pressure is fixed at 12 MPa. Engine speed is varied from 1000 rpm to 4500 rpm, and optimal single injection timing is found via a sweep at each load. Split injection, it is only carried out between 1500 rpm and 3500 rpm since the short interval between injections mean that the effects of split injection are negligible at high speed. The important split injection control parameters of start of injection (SOI), split end of injection (SEOI) and split injection mass proportion (SIMP) are indicated in Fig. 2 respectively,

Table 3 Summary of experimental operations and performance comparisons

Parameters	Single injection	Split injection
Engine speed (rpm)	1000 to 4500	1000 to 3500
SOI (°CA-BTDC)	80 to 180	80 to 160
SEOI (°CA-BTDC)	NA	20 to 55
SIMP (%)	NA	10 to 60
Spark timing (°CA-BTDC)	-2.5 to 15	-2.5 to 15
Maximum Brake Power	124.8 kW @ 4500 rpm	71.8 kW @ 3500 rpm
Maximum BTE	42.53 % @ 2500 rpm	43.03 % @ 2500 rpm
Intake absolute pressure	220 kPa	220 kPa
Cooling Temperature	358 K	358 K

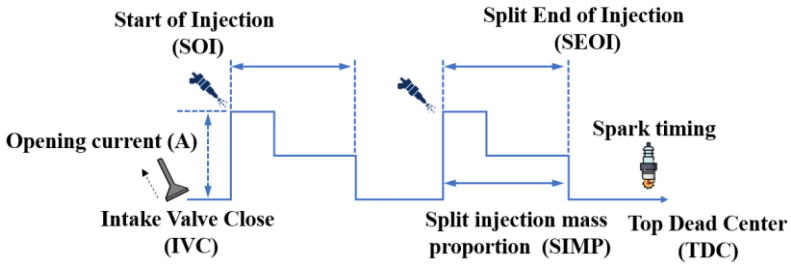


Fig. 2 Schematic diagram of split injection

2.3 Numerical models

Fig. 3 shows the geometry and grid parameters of the 3D model. The computational domain of the engine model is set as a 4 mm base grid. Different mesh strategies and levels are used for different areas on this hydrogen engine model as shown in Table 4. The grid size after n levels of refinement is $dx_{base}/2^n$ mm, where dx_{base} is the basic grid size of a cell after being refined by multiple refinement strategies, with the highest level being taken as the example. The combustion chamber is refined using adaptive refinement based on velocity and temperature gradients, with a maximum of five levels of refinement. The maximum grid size within the refined combustion chamber does not exceed 0.5 mm to ensure that the flame development process is captured. The grid near the spark plug is refined to 0.125 mm to ensure that the model can accurately predict the formation and development of the fire kernel. Additionally, the grid near the hydrogen nozzle is also refined for better observation of the jet morphology during hydrogen injection and to analyze the state of mixture formation in the cylinder. Finally, to accurately simulate the hydrogen injection process, the inner part of the hydrogen nozzle and the vicinity of the outlet are refined to 0.25 mm and 0.5 mm, respectively.

The coupling of turbulence and combustion effects undoubtedly increases the difficulty of numerical simulation. In this study, the RNG-RANS method is selected to obvious the turbulence characteristics. [30].

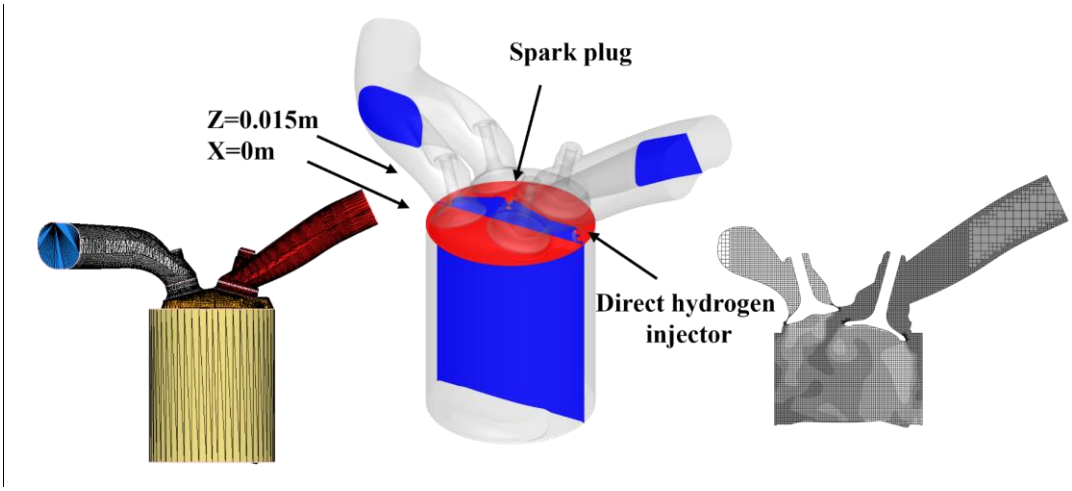


Fig. 3 Hydrogen engine computation domain and meshing

Table 4 Mesh distribution and local refinement

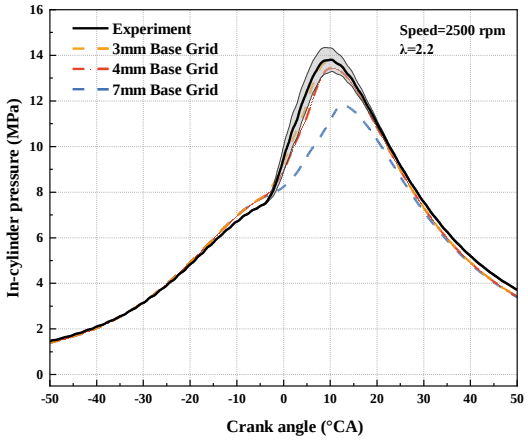
Regions	Mesh strategies	Refinement period	Mesh size
Combustion chamber	Fixed embedding/5	Full cycle	0.5 mm
Intake and exhaust valves	Fixed embedding/5	Full cycle	0.25 mm
Injector internal flow path	Fixed embedding/4	Full cycle	0.5 mm
Injector nozzle	Fixed embedding/3	Injection duration	1 mm
Spark plug	Fixed embedding/5	−15°CA ~10°CA	0.25 mm
Spark plug electrode	Fixed embedding/6	−15°CA ~10°CA	0.125 mm
Near the injector	Hydrogen concentration AMR/3	Injection duration	0.125 mm

2.4 Numerical model validation

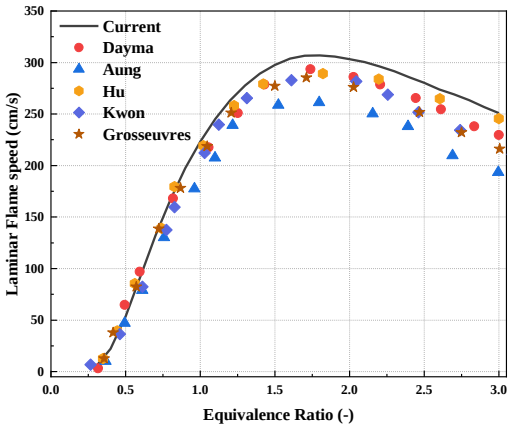
Engine model validation

The grid independence test results are shown in Fig. 4(a). It can be seen that the results of the 3mm and 4mm base grid models are similar. However, there is a big difference between the 7 mm grid and the 3 mm grid. Taking into account simulation time, 4 mm is chosen as the base gird. In addition, evaluating the in-cylinder pure hydrogen combustion process is important. The combustion model is SAGE model and the validation of laminar flame velocity of reaction mechanisms is shown in Fig. 4(b) [31–35]. Moreover, hydrogen injection is a crucial process for forming the air-hydrogen mixture. To validate the simulation, high-pressure hydrogen injection is measured inside a constant volume chamber. Experimental results are obtained

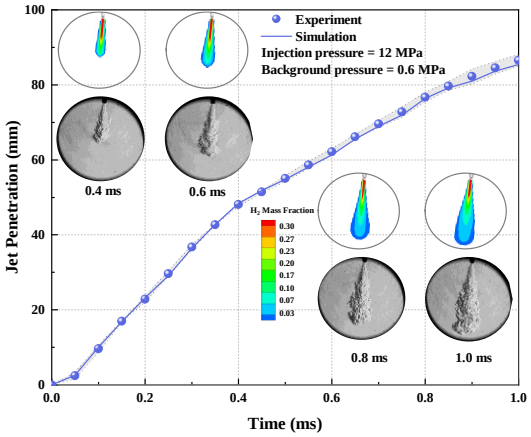
using a high-speed schlieren photography system at an injection pressure of 12 MPa, a background pressure of 0.6 MPa, and a temperature of 297 K. A three-dimensional model of the constant volume chamber is established, and the Re-Normalization Group (RNG) k-ε model is employed for simulation. The simulation results are compared with experimental data, as shown in Fig. 4 (c) [36]. In terms of hydrogen injection development, the jet penetration reflects spray diffusion, and the simulation's jet penetration data are found to be within the experimental error range. [14]



(a) Base grid selection



(b) Validation of laminar flame velocities.

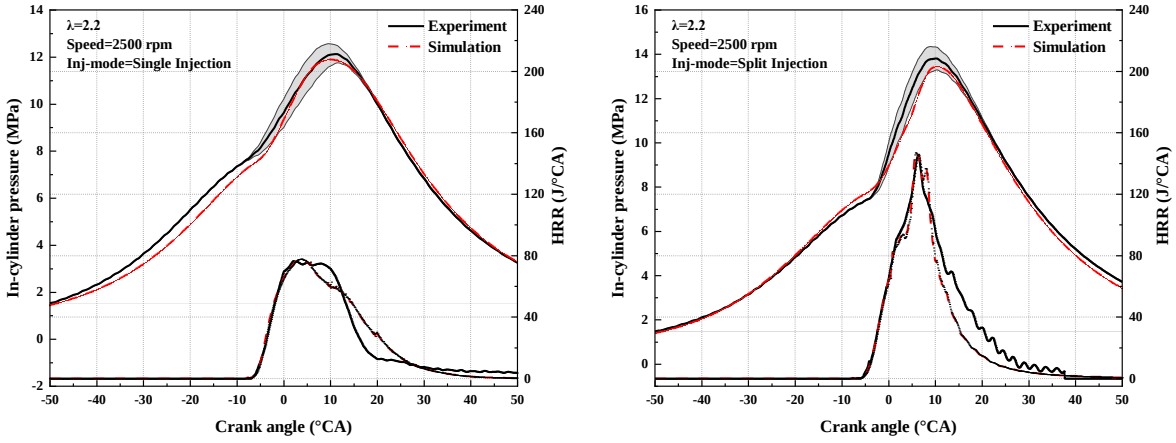


(c) Validation of jet penetration

Fig. 4 Engine model validation

Experimental data of in-cylinder pressure and heat release rate (HRR) with different injection modes

are used to validate the engine model. Fig. 5 shows the comparison between the numerical and the experimental data at the engine speed of 2500 rpm, λ=2.2, and injection mode of single and split, respectively. The grey area in Fig. 5 represents the standard deviation of in-cylinder pressure over the 200 cycles of the experiment. The in-cylinder pressure and heat release rate accurately replicate the experimental data. The simulation errors for both injection modes are consistently below 5%. In summary, the model developed in this study demonstrates excellent predictive capability for assessing the performance of hydrogen engines under different injection modes.



(a) Validation of Single injection (b) Validation of Split injection

Fig. 5 Comparison of simulation and experiment results of In-cylinder pressure and heat release rate

Simulation conditions

To investigate the effects of mixture formation and combustion characteristics on engine performance, the test conditions varied the engine speed from 1500 rpm to 4500 rpm, with a constant hydrogen injection pressure of 12 MPa. Within the range of 1500 rpm to 3500 rpm, split injection tests were conducted and compared with single injection. Additionally, numerical simulations were performed for operating conditions of abnormal combustion and the highest efficiency to validate the experimental data with the in-cylinder flow, mixture formation, and flame propagation processes. The numerical validation cases are shown in Table 5

Table 5 Operating conditions of simulation cases

Cases	Injection mode	Hydrogen mass flow	SOI	EOI	SSOI	SEOI	SIMP
-	-	mg/cycle	°CA	°CA	°CA	°CA	%
1	Single-Inj	9.52	-100	-67	-	-	0
2	Single-Inj	9.52	-80	-47	-	-	0
3	Split-Inj	9.52	-100	-79	-41	-30	35
4	Single-Inj	14.82	-100	-55	-	-	0
5	Split-Inj	14.82	-100	-67.5	-43	-25	35

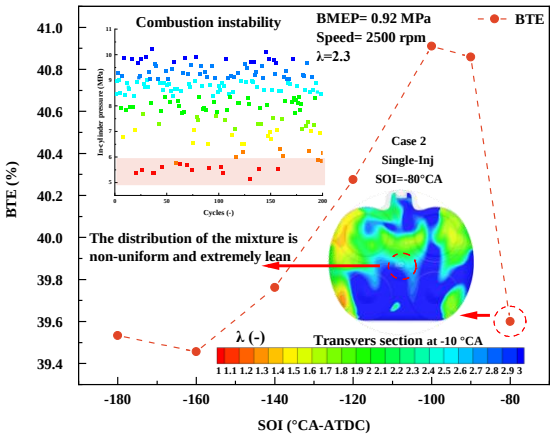
3. Results and discussion

3.1 Combustion characteristics of single and split injection

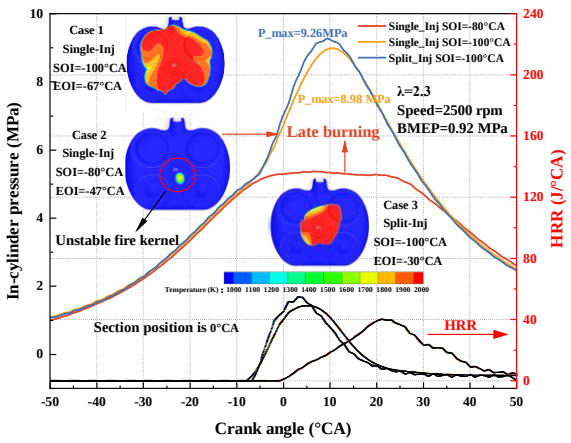
Effects of SOI of single injection on engine performance are first studied experimentally. The engine speed is set at 2500 rpm with full throttle. Hydrogen injection pressure is set at 12 MPa, with a fixed hydrogen injection mass of 9.52 mg per cycle. At low injection pressures (e.g., 6 MPa), the injection pulse width is longer, and an improper split injection mass proportion (SIMP) can cause interference between the start of the secondary injection and the end of the first injection. This makes effective split injection difficult to achieve under high-load, high hydrogen flow conditions. On the other hand, excessively high injection pressures (e.g., 18 MPa) reduce the available hydrogen in the tank, shortening the effective experiment time and limiting the ability to collect and validate extensive data. Additionally, the hydrogen pipeline in the lab can only withstand up to 18 MPa. Therefore, for safety and experimental effectiveness, we selected a moderate injection pressure of 12 MPa for the experiments. The ignition angle is set at -10 °CA, and the SOI was adjusted from -180 °CA to -80 °CA.

As shown in Fig. 6(a), as the SOI of single injection approaches the top dead center (TDC), BTE

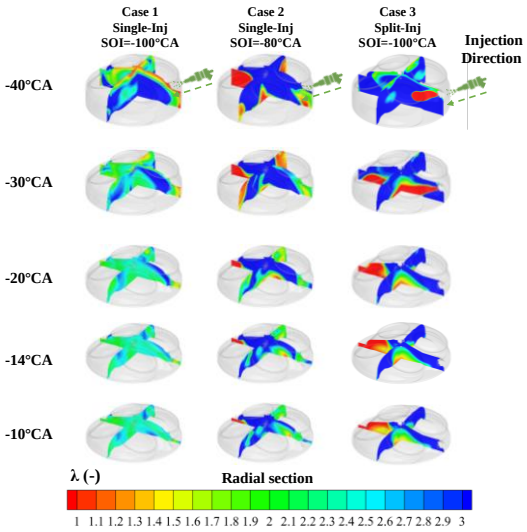
gradually increases from 39.53% with SOI=-180 °CA to 40.02% with SOI=-100 °CA. Appropriate late injection timing leads to the reduction of compression energy loss and pumping loss with increasing thermal efficiency [28,37–39] . However, when the SOI moves to -80°CA, unstable combustion occurs with a decreasing BTE of 39.36%. Analysis of the in-cylinder pressure of 200 continuous cycles at SOI=-80 °CA indicates that the peak pressure of 16 late burning cycles around 5.12 MPa to 5.77 MPa, which is lower than the average of 8.24 MPa. The numerical results demonstrate that an improper EOI could result in a non-uniform mixture distribution, where the mixture near the spark plug is excessively lean (λ>2.5). This condition lead to the formation of an unstable fire kernel at the moment of ignition, impeding the flame propagation process, as depicted in Fig. 6 (b). Consequently, a significant proportion of the mixture will be ignited after TDC, leading to late burning [37]. The distribution of λ for different injection timings and injection modes is shown in Fig. 6 (c) and (d). With an SOI of -100 °CA, a homogeneous mixture with λ = 2 is formed near the spark plug. However, when the SOI is delayed to -80 °CA, the mixture becomes non-uniform and extremely lean (λ > 2.5) at the spark timing of -10 °CA. Additionally, under split injection mode (Case 3), the mixture near the spark plug shows stratification, with λ ranging from 1.1 to 2.1. This stratification improves the stability of the fire kernel formation and helps prevent abnormal combustion.



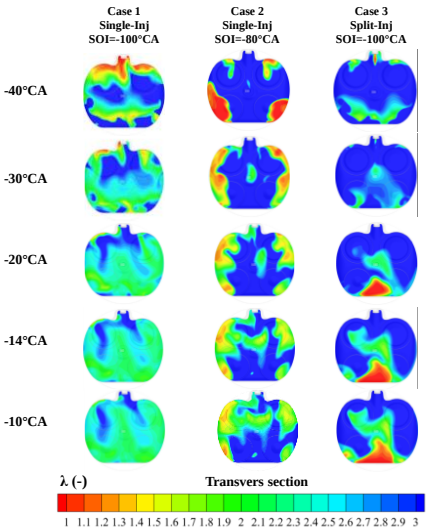
(a) Effect of single injection timing on the BTE



(b) Comparison of single and split injection mode of combustion characteristics



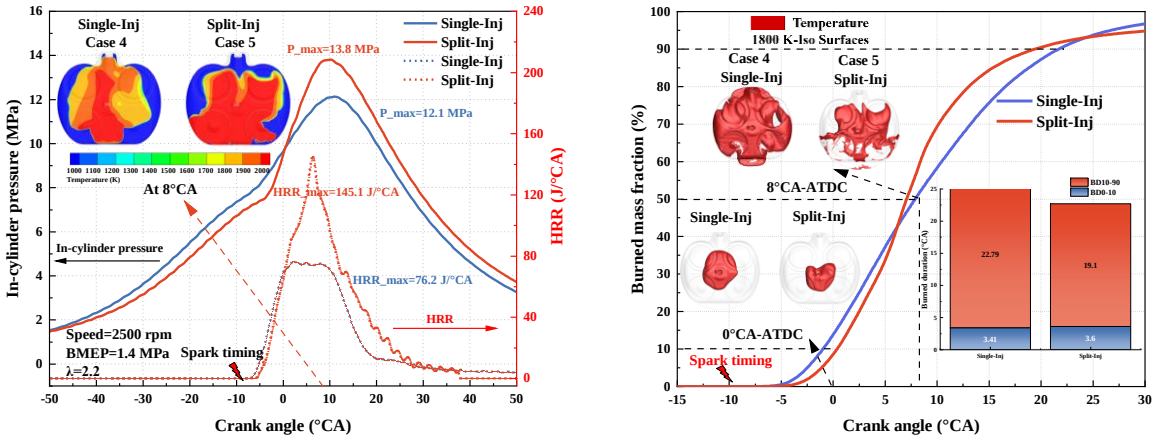
(c) The mixture distribution various with Crank Angle-Racial section



(d) The mixture distribution various with Crank Angle-Transver section

Fig. 6 Effect of injection timing on the in-cylinder pressure, HRR, and mixture distribution

Further investigations of the maximum BTE operating conditions with different injection modes are carried out. Fig. 7 compares the combustion characteristics of single injection (Case 4) and split injection (Case 5). The hydrogen mass flow is increased to 14.82 mg/cycle hence λ decreased from 2.3 to 2.2. Meanwhile, the corresponding air mass flow increase from 225 kg/h to 337 kg/h after the turbocharging. As show in Fig. 7 (a), the maximum in-cylinder pressure of split injection reaches 13.8 MPa, which is 1.7 MPa higher than that of single injection. The maximum HRR of split injection reaches 145.1 J /°CA results in a large combustion area in the center of cylinder. As illustrated in Fig. 7 (b), the ignition delay (BD 0-10) of Case 4 is 0.19 °CA shorter than that of split injection. Moreover, the burn duration (BD 10-90) of Case 5 reaches 19.1 °CA, which is 3.69 °CA shorter than Case 4. Additionally, comparing the combustion center (CA50), Case 5 is at 7.1 °CA, which is 0.8 °CA advanced than that of Case 4. The combustion temperature of Case 5 is higher than that of Case 4, and the high-temperature region is more concentrated in the center of the cylinder. Thus, split injection increases the flame speed and results in high combustion efficiency in this case.



(a) In-cylinder pressure, HRR and BTE (b) Burned mass fraction and burned duration

Fig. 7 Experimental comparison of BTE, In-cylinder pressure and HRR of different injection modes.

The numerical study reflects the differences between the two injection modes. Fig. 8 presents the evolutions of in-cylinder λ distribution from -40 °CA to the spark timing. For the single injection, a global of λ=2.2 homogeneous mixture is formed, and rich mixture of λ=2 mainly gathers on the both sides of cylinder wall. In terms of split injection, an ultra-rich region (λ<1.2) of hydrogen is concentrated near the cylinder wall opposite the injector. Fortunately, the spark plug electrode is surrounded by a uniform mixture, which is influenced by the tumble parallel to the hydrogen jet direction. The lean mixture of λ exceeds 2.6 is seen near the cylinder wall with split injection.

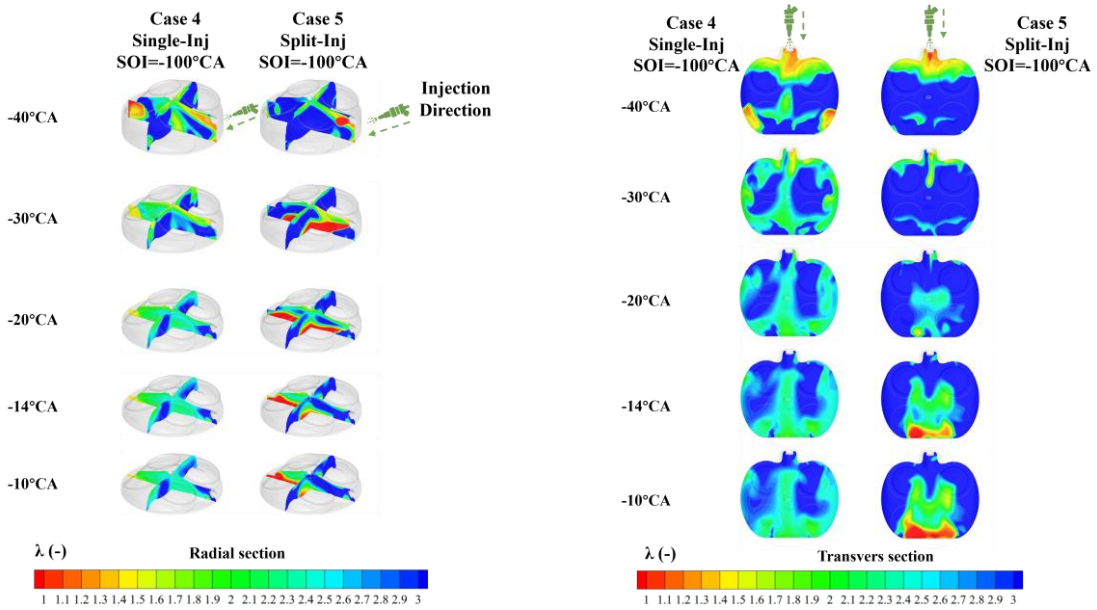
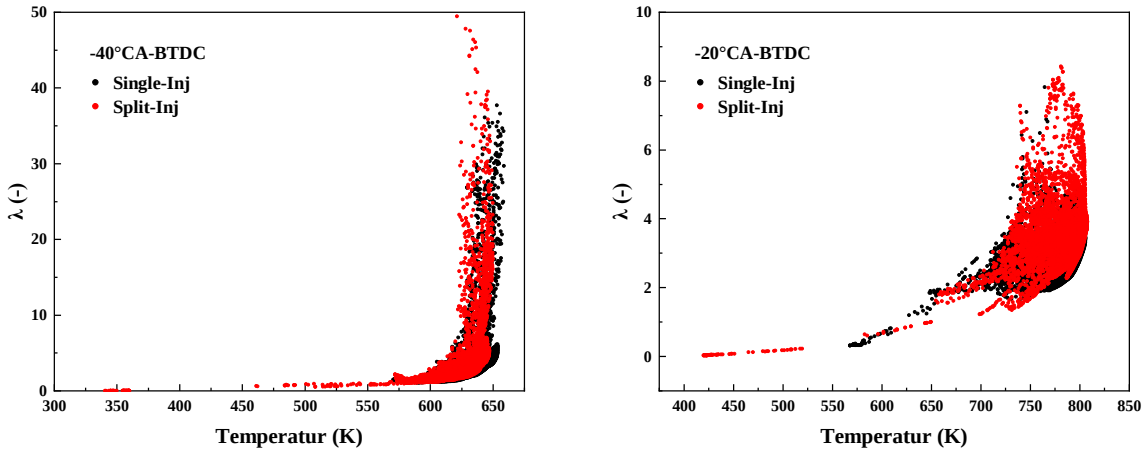


Fig. 8 The distribution of the λ with different injection modes

Fig. 9 illustrates the probability density distribution of λ and corresponding temperature during the mixing and early stage of the combustion process. The differences between the two injection modes are not significant at -40°CA and -20°CA. However, the λ distribution of single injection is mainly clustered between 2 and 3 after -10°CA, with the temperatures of major areas exceeding 800 K, providing conditions for smooth flame development. In contrast, the λ distribution of split injection shows clear stratification. It ranges from ultra-rich to ultra-lean regions, covering the temperature range from 700 K to 900 K. The richer mixture (λ<1.5) mainly concentrates in the temperature range below 800 K, and λ corresponding to 850 K temperature of split injection is lower than under the single injection mode. Therefore, the split injection mode gathers a richer and higher-temperature mixture near the spark plug. The reasons for this stratification can be explained by the fact that split injection can delay SEOI, causing less turbulent kinetic energy (TKE) to be introduced by the injection. The mixing time is shortened by split injection, which promotes the formation of a richer mixture near the spark plug [40].



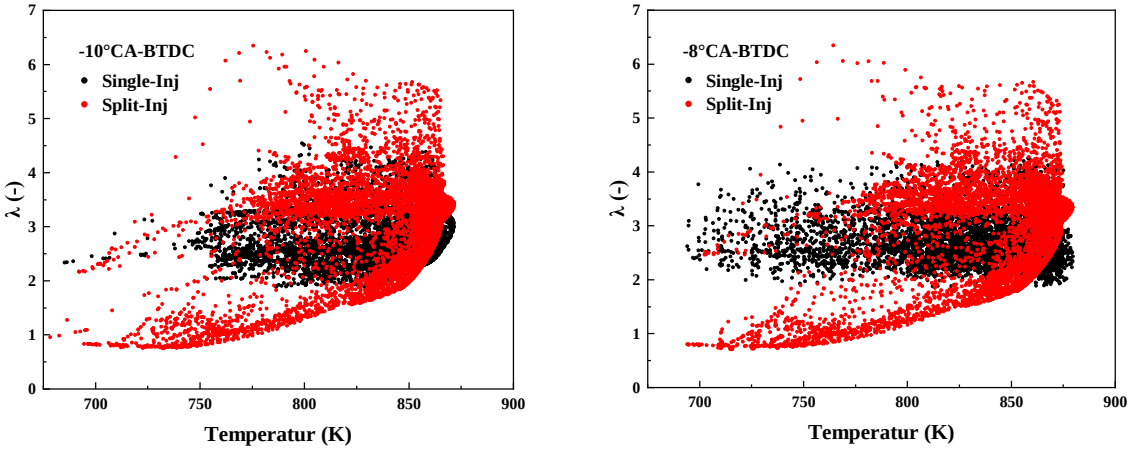
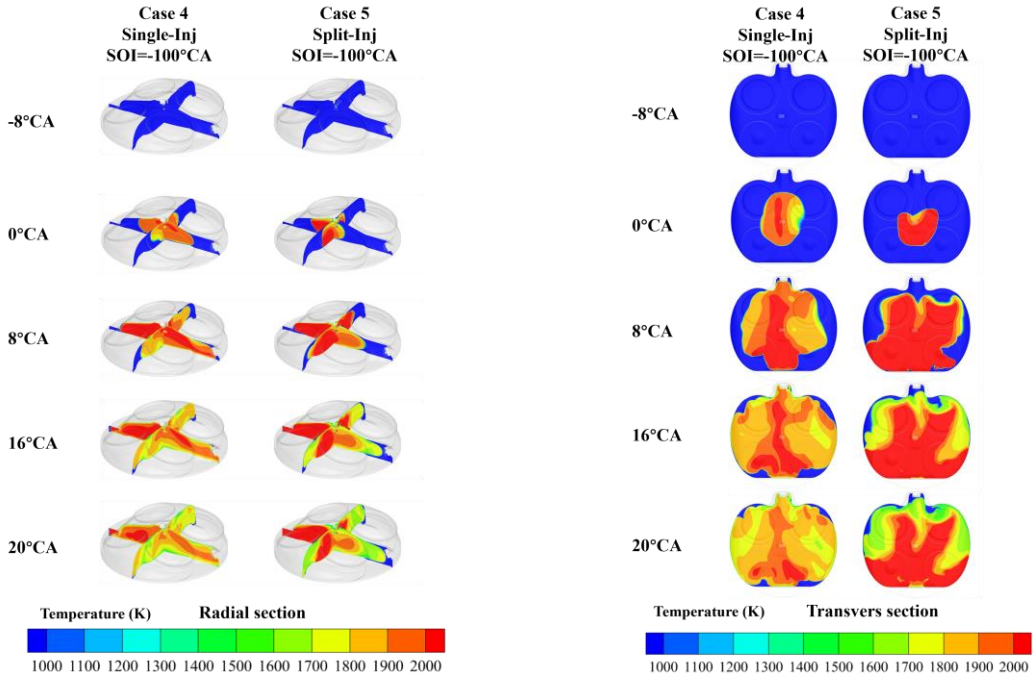


Fig. 9 The scatter of λ and temperature at different crank angles

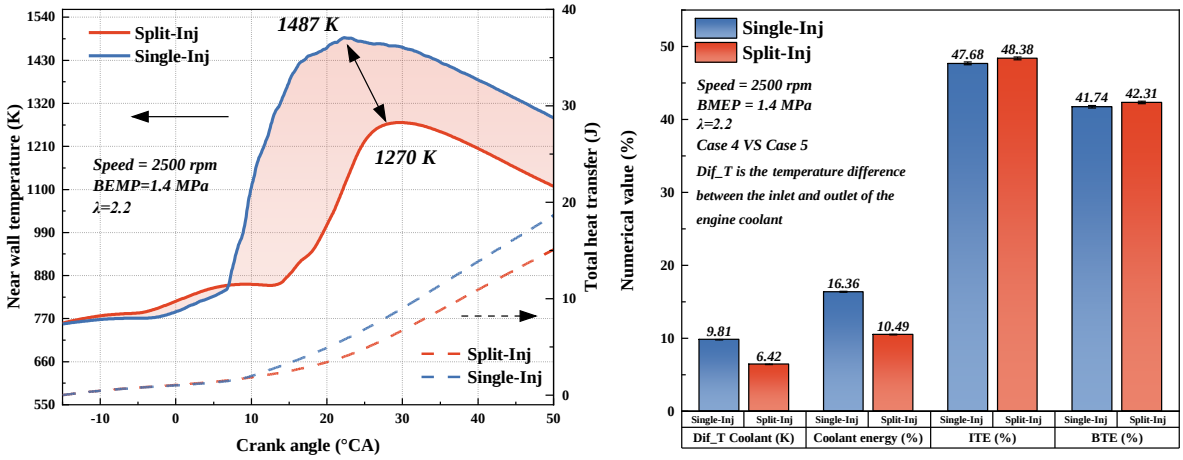
As shown in Fig. 10, the flame kernels first form around the spark plug electrode at -8°CA. As the flame develops, the temperature of over 80% of the burned zone reaches 2000 K at 0°CA with split injection. In contrast the flame front temperature of the single injection ranges from 1700 K to 1900 K, and only the core region reaches 2000 K. For the split injection, the cylinder temperature continues rising and a high-temperature region of 2500 K is formed near the exhaust valves, which is significantly larger than that with single injection. The temperature near the wall of the intake side remains at around 1700K in an ultra-lean mixture region (λ>2.5) - thus, more concentrated and higher combustion temperature and in-cylinder pressure results in a higher BTE with split injection [20].



(a) Radial section (b) Cross section

Fig. 10 The distribution of in-cylinder temperature with different injection modes

The above deduction of low heat transfer loss is also been demonstrated by numerical and experimental results shown in Fig. 11. As shown in Fig. 11(a), the maximum near-wall average temperature of the single injection case reaches 1487 K, which is 217 K higher than that of the split injection case. This results in the total heat transfer of the single injection case being 18.64 J at 50 °CA, which is 3.56 J higher than that of split injection. According to the test results in Fig. 11(b), the coolant temperature difference and coolant energy of split injection reaches 6.42 K and 10.49% respectively which are lower than that of single injection. Consequently, the ITE of split injection reaches 48.38% and the BTE results in 42.31%, which is 0.57 percentage points higher than that of single injection.



(a) Near wall temperature-Numerical results (b) Energy distribution-Experimental results

Fig. 11 Effects of heat transfer on ITE and BTE

3.2 Effect of single and split Injection on engine performance

Further tests are conducted to investigate the single-factor effects of injection strategy on engine performance at different speeds and loads. As shown in Fig. 12, split injection achieves a higher efficiency at all conditions, with the BTE increasing by 0.93 percentage points, 1.25 percentage points, and 1.01 percentage points at 1500 rpm, 2500 rpm, and 3500 rpm, respectively. The maximum improvement of BTE is observed at 2500 rpm with higher mechanical efficiency compared to other speeds. Moreover, with increasing engine speeds, the optimal spark timing corresponding to the peak efficiency occurs progressively later.

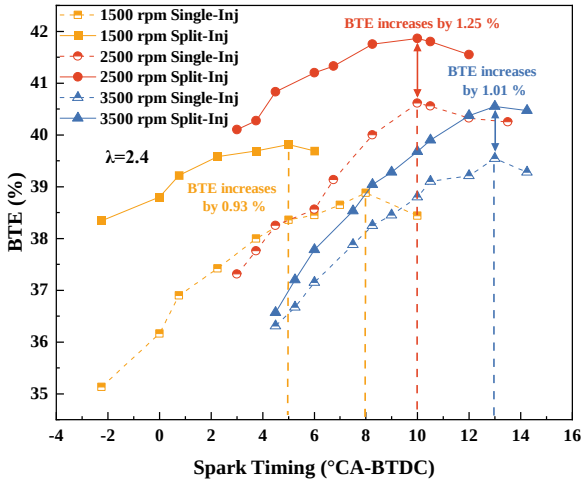


Fig. 12 Effect of spark timing on BTE various with engine speeds and injection modes

Fig. 13 shows a comparative assessment of combustion characteristics between single and split injection modes. For instance, at the engine speed of 2500 rpm with a spark timing of 10 °CA -BTDC, the center of combustion (CA50) for the split injection strategy is positioned at 6 °CA, which is advanced by 3.6°CA relative to the single injection mode. Additionally, the combustion duration (BD10-90) is reduced to 21.59°CA under the split injection mode, a decrease of 1.23°CA compared with the single injection mode. The positioning of the combustion center closer to the TDC and the shorter combustion duration under the split injection mode are associated with higher in-cylinder pressures, temperatures and HRR. Specifically, these parameters of split injection mode have been observed to increase by 0.82 MPa, 90 K, and 9.68 J/°CA, respectively, compared to the single injection mode. However, the increasing combustion temperatures and the rising formation of locally rich mixtures within the split injection mode result in higher NOx emissions as compared to the single injection mode.[15]

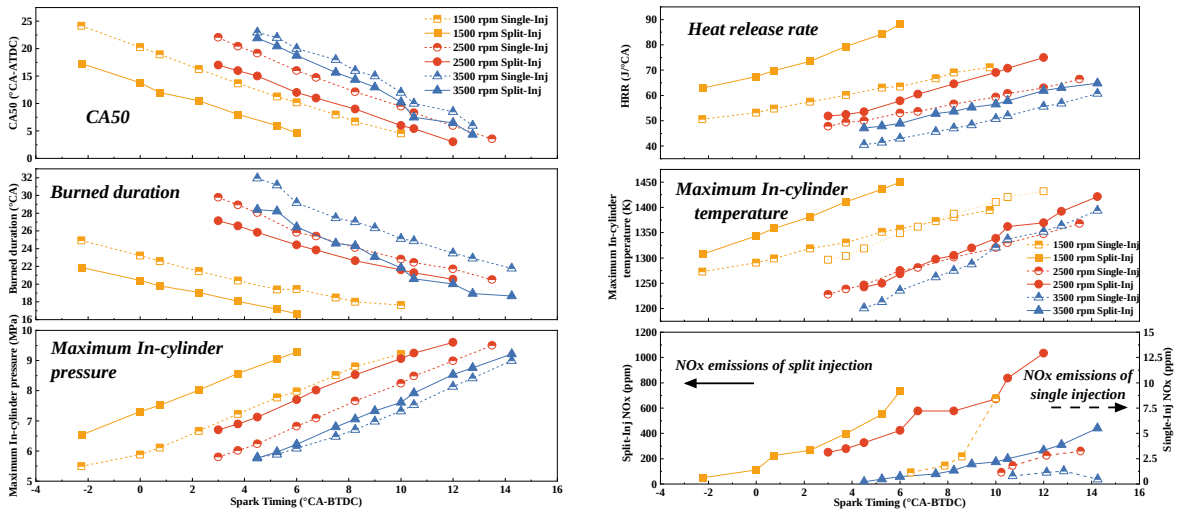
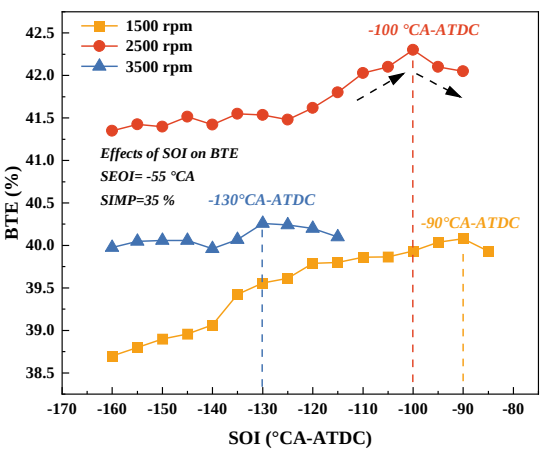
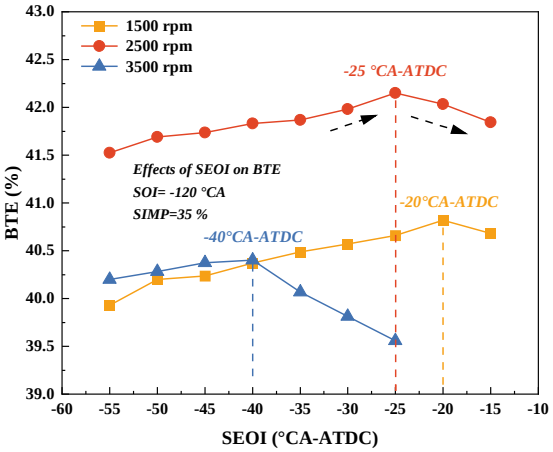


Fig. 13 Combustion and emissions characteristics of the different injection modes

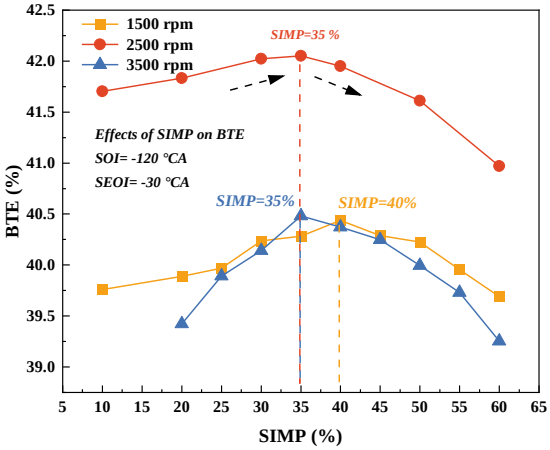
As shown in Fig. 14, experiments were conducted to study the single-factor effect of three injection control parameters (SOI, SEOI and SIMP) on BTE at different engine speeds with a constant λ of 2.4. The turning point of each factor is observed during the adjustments. As engine speeds increase, the optimal SOI phase is put forward from -90°CA to -130°CA, the best SEOI is advanced from -20°CA to -40°CA, and the peak SIMP keeps constant around 35%. The advancement of SOI and SEOI aims to prevent excessively rich mixtures at the spark timing, which may lead to pre-ignition and knock. The BTE of 2500 rpm is the highest among all engine speed conditions which exceeds 42%. Moreover, the interaction effects are detected because all three parameters impact the cylinder in-flow and mixture distribution simultaneously. To achieve a higher BTE with low NOx emissions, a multi-parameter optimization is conducted at the engine speed of 2500 rpm in the following section.



(a) Start of the first injection



(b) Split end of injection



(b) Split injection mass proportion

Fig. 14 Effect of split injection parameters on BTE

3.3 Multi-parameter optimization of split injection and spark timing based on the RSM method

Response Surface Methodology (RSM) allows for a thorough understanding of the relationships between multiple variables and their impact on the system's performance. In Section 3.2, sequential experiments on split injection parameters and spark timing were conducted, and the central points of SOI=-100 °CA, SEOI= -25 °CA, SIMP=35% and CA50=6 °CA were obtained. In a series of experimental designs consistent with RSM, the Central Composite Design (CCD) is the preferred choice with high effectiveness and comprehensive applicability. For the CCD experimental setup, SOI, SEOI, SIMP and CA50 are considered as factors (input variables), whereas BTE, NOx emissions and maximum amplitude of pressure

(MAPO) are the response variables. Table 6 illustrates the random sequence of CCD design and experimental data of 28 tests, a maximum BTE of 43.06% is achieved in test No.6.

Table 6 CCD design and engine test data

Test No.	SOI	SEOI	SIMP	CA50	BTE	NOx	MAPO
	°CA	°CA	%	°CA	%	ppm	MPa
1	-90	-35	45	2	41.92	1860	0.06
2	-90	-35	25	10	42.95	719	0.02
3	-110	-35	45	10	42.91	1132	0.02
4	-110	-35	25	2	42.01	1553	0.02
5	-110	-15	45	2	42.06	1511	0.08
6	-100	-25	35	6	43.06	1425	0.04
7	-110	-15	25	10	42.29	1075	0.03
8	-100	-25	35	6	42.95	1497	0.03
9	-90	-15	45	10	42.49	1057	0.07
10	-90	-15	25	2	42.11	1361	0.06
11	-110	-35	25	10	42.67	781	0.02
12	-110	-15	45	10	42.41	1092	0.06
13	-90	-15	25	10	42.51	1006	0.04
14	-100	-25	35	6	42.95	1460	0.04
15	-110	-15	25	2	41.65	1397	0.05
16	-90	-15	45	2	42.35	1464	0.09
17	-100	-25	35	6	42.97	1424	0.03
18	-90	-35	45	10	42.61	1264	0.03
19	-90	-35	25	2	42.28	1494	0.03
20	-110	-35	45	2	42.52	2047	0.03
21	-100	-45	35	6	42.64	1300	0.06
22	-120	-25	35	6	42.69	1497	0.03
23	-100	-5	35	6	41.21	558	0.07
24	-100	-25	35	-2	41.45	2222	0.06
25	-100	-25	35	6	42.94	1494	0.03
26	-100	-25	35	6	42.98	1474	0.04
27	-80	-25	35	6	42.88	1527	0.05
28	-100	-25	55	6	42.95	1593	0.04

A second-order polynomial equation is used to predict the output response. Table 7 shows the analysis of variance (ANOVA) results for the response values derived from experimental data. The model's F-value surpasses the critical value of 2.92, indicating a statistical significance. Furthermore, the insignificant terms

are eliminated with the F-test. Validating the model's efficacy in explaining the response variables' variance and a high R^2 is achieved for three models [41].

Table 7 The ANOVA for the response surfaces of the three models.

Source	BTE model		NOx model		MAPO model	
	F-value	P-value	F-value	P-value	F-value	P-value
Model	17.95	<0.0001	46.59	<0.0001	11.12	<0.0001
A-SOI	1.29	0.27	-	-	6.74	0.016
B-SEOI	26.02	<0.0001	24.87	<0.0001	29.07	<0.0001
C-SIMP	1.06	0.316	23.06	<0.0001	14.4	0.001
D-CA50	35.8	<0.0001	220.08	<0.0001	14.4	0.001
B^2	49.51	<0.0001	69.46	<0.0001	13.03	0.002
D^2	52.94	<0.0001	-	-	-	-
AC	5.12	0.035	-	-	-	-
BC	-	-	14.36	0.001	-	-
BD	-	-	16.05	0.001	-	-
R^2	88.98%		94.67%		77.96%	
Adj-R^2	84.03%		92.64%		70.95%	

Based on the experimental data, the regression equations representing BTE, NOx emissions, and MAPO are as follows:

$$\mathrm{BTE}\ (\%) = 44 + 0.0430 * \mathrm{A} - 0.1485 * \mathrm{B} - 0.1059 * \mathrm{C} + 0.2584 * \mathrm{D} - 0.002566 * \mathrm{B}^2 - 0.01658 * \mathrm{D}^2 - 0.001100 * AC \quad (5)$$

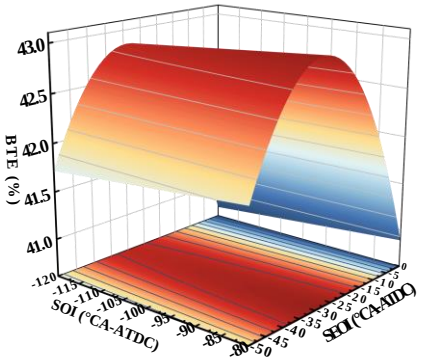
$$\mathrm{NO}_x\ \mathrm{emission}\ (\mathrm{ppm}) = 837 - 67.6 * \mathrm{B} - 13.47 * \mathrm{C} - 12.7 * \mathrm{D} - 1.507 * \mathrm{B}^2 - 0.919 * \mathrm{BC} + 2.430 * BD \quad (6)$$

$$\mathrm{MAPO}\ (\mathrm{MPa}) = 0.1469 + 0.000542 * \mathrm{A} + 0.004562 * \mathrm{B} + 0.000792 + \mathrm{C} - 0.001979 * \mathrm{D} + 0.0000687 * \mathrm{B}^2 \quad (7)$$

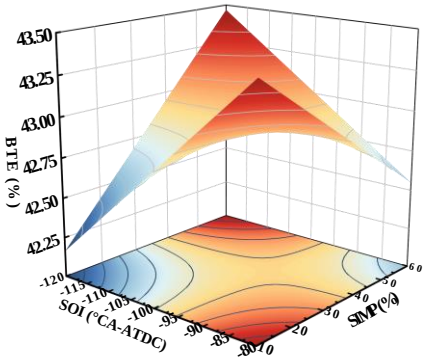
Where A is the SOI, B is the SEOI, C is the SIMP and D is the CA50.

Fig. 15, Fig. 16, and Fig. 17 present the three-dimensional response surface plots that depict the interactive effects of the four input variables on the three response variables. The colour gradients and elliptical contours signify substantial interactions among the factors. Fig. 15 indicates significant interactions between split injection control parameters and CA50. This result displayed in Fig. 15 (a) and (d) reflects that when the SEOI lies between -40 °CA and -20 °CA, a high BTE of over 42% is reached. Fig. 15 (b) shows

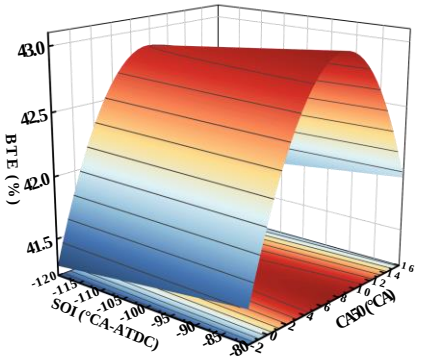
that raising SIMP to 60% results in decreased BTE with poor mixture formation. Split injection can achieve a higher level of turbulence, but a higher SIMP (which makes split injection trend towards single injection) will weaken the stratification of the mixture formed by the split injection, and reduce the combustion efficiency [22,42]. Fig. 15 (c), (e) and (f) depict the effects of spark timing; maintaining the CA50 at 6 °CA leads to a higher BTE due to the rapid flame propagation velocity, which results in a quicker combustion process [43]. In addition, the results also illustrate that the MBT (Minimum Spark Advance for Best Torque) point corresponds to CA50=6°CA at 2500 rpm.



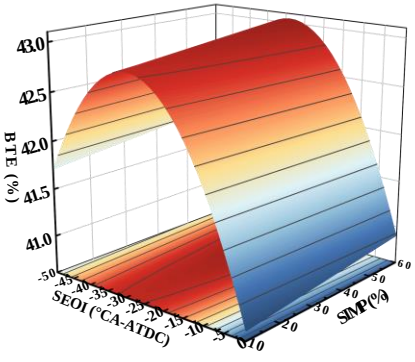
(a) SOI-SEOI



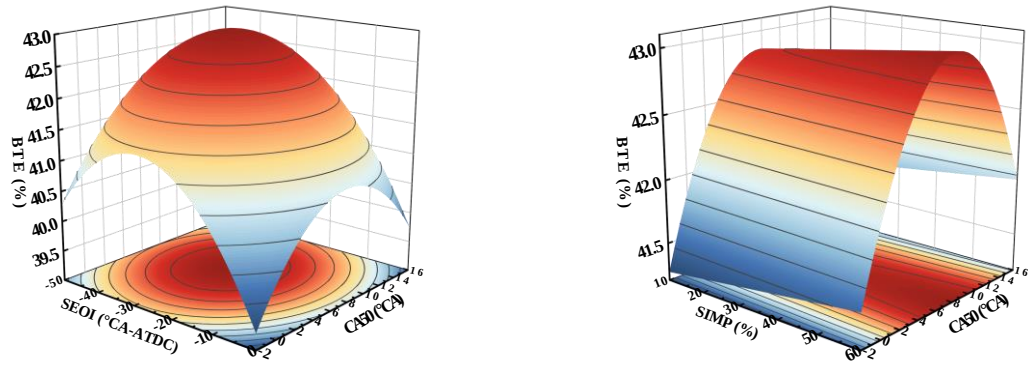
(b) SOI-SIMP



(c) SOI-CA50



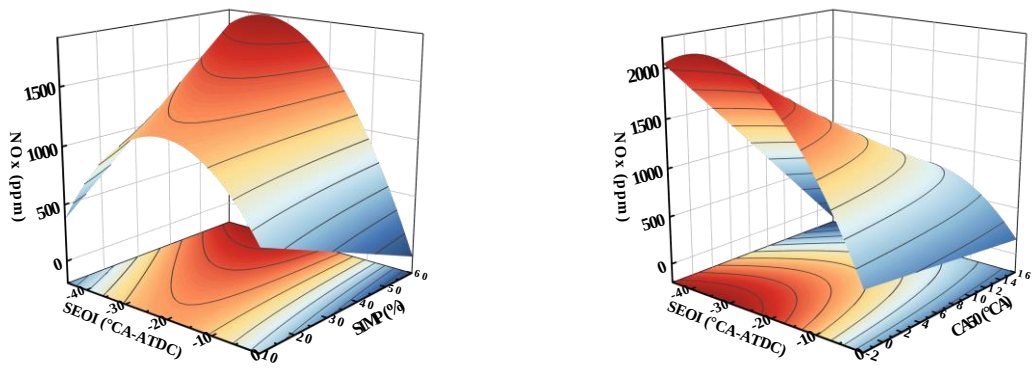
(d) SEOI-SIMP



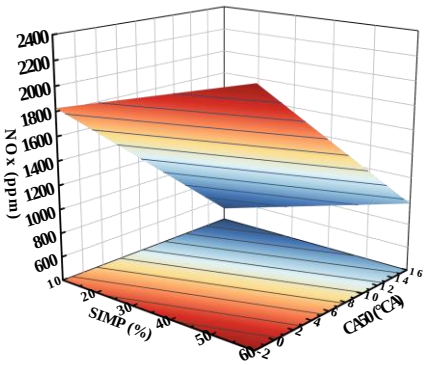
(e) SEOI-CA50 (f) SIMP-CA50

Fig. 15 Response surface of the influence of split injection and spark on the BTE

Fig. 16 illustrates the impact of SEOI, SIMP and CA50 on NOx emissions since SOI is regarded as an insignificant factor after the ANOVA. As shown in Fig. 16 (a), NOx emission increases first and then decreases as SEOI approaches the TDC. A NOx emission of less than 500 ppm is obtained if SEOI is set earlier than -40 °CA. Moreover, the NOx emissions exceed 1500 ppm when the SIMP is set at 60%, as most hydrogen is injected near TDC. This leads to a rapid increase in combustion temperature, thereby enhancing the formation of thermal NOx. Fig. 16 (b) illustrates that the impact of SEOI on NOx formation is markedly higher than that of CA50, as the mixture distribution is predominantly influenced by SEOI. Additionally, Fig. 16 (c) demonstrates that higher SIMP and CA50 closer to TDC are correlated with increased NOx emissions. The most significant and rapid method of heat transmission is flame radiation, which is accelerated by CA50. The flame produces hot-spot areas that are qualifying zones for NOx generation [9].



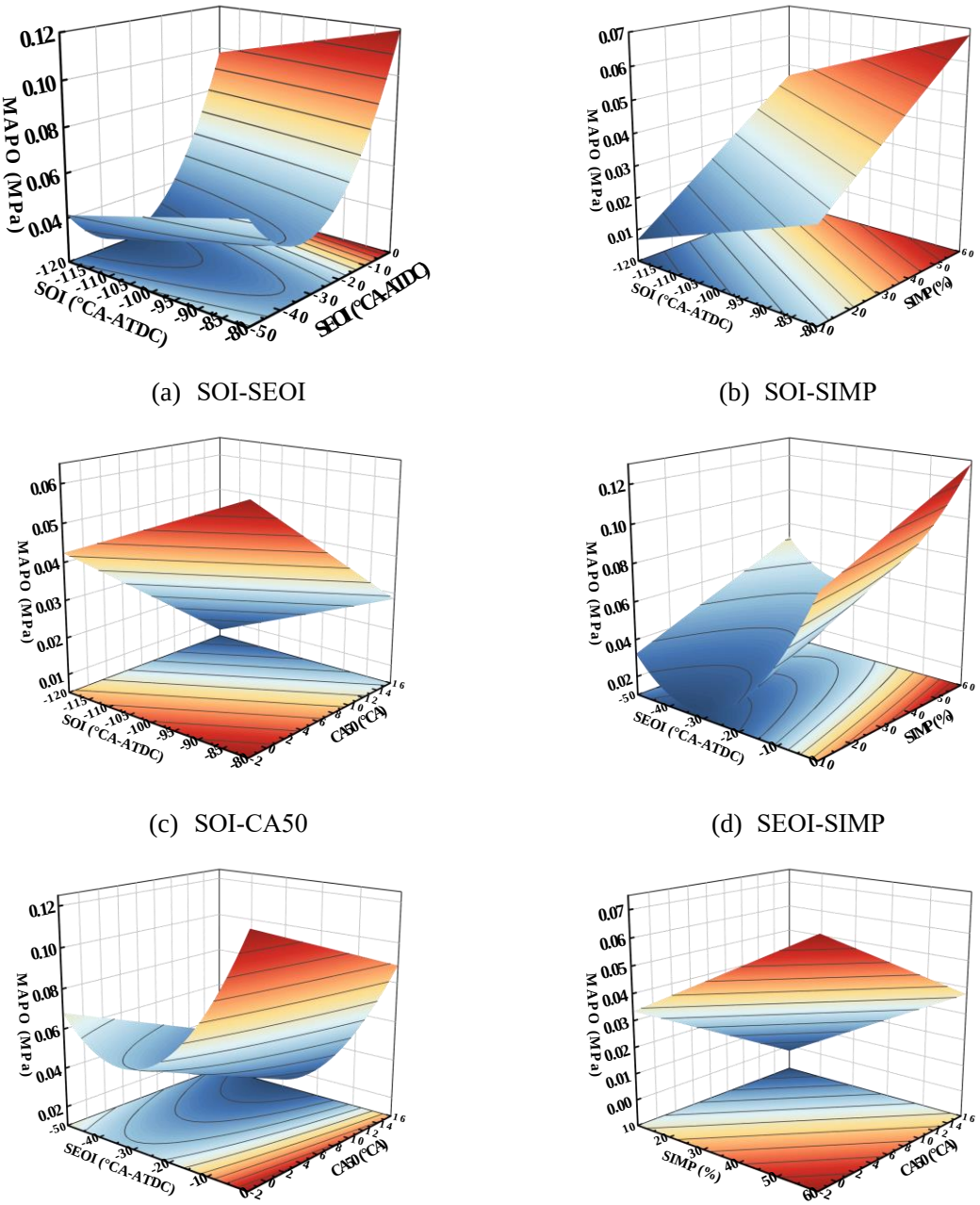
(a) SEOI-SIMP (b) SEOI-CA50



(c) SIMP-CA50

Fig. 16 Response surface of the influence of split injection and spark on the NOx emissions

Fig. 17 illustrates that all split injection control parameters and CA50 significantly affect the MAPO. The MAPO presents the tendency and intensity of knock, and the threshold value of MAPO is set as 0.1 MPa [44]. Fig. 17 (a), (b) and (d) demonstrate that MAPO increases rapidly as SEOI is later than -15°CA, and SIMP higher than 40%, with a spark timing of CA50=6°CA. Delayed SEOI and increased SIMP lead to rich mixtures gathering in the triangular regions of the slanted roof combustion chamber. The rich mixture near the cylinder wall tends to auto-ignite due to the heat from the burned gases and piston compression. Fig. 17 (c), (e) and (f) illustrate the impact of spark timing on MAPO which is more significant than injection. Ignition near TDC results in the highest peak cylinder pressures. The pressure wave interacts with the flame front hindering its spread to unburned areas, leading to end-gas auto-ignition and knock [45,46]. Consequently, CA50 might best be delayed to after 6°CA to avoid knock.



(a) SOI-SEOI (b) SOI-SIMP

(c) SOI-CA50 (d) SEOI-SIMP

(e) SEOI-CA50 (f) SIMP-CA50

Fig. 17 Response surface for the influence of split injection control parameters and CA50 on MAPO

Multiple objective optimizations are conducted based on the RSM model to achieve the highest BTE, lowest NOx emissions and lowest MAPO. As shown in Fig. 18, a composite desirability coefficient of 0.8925 is achieved, optimal response levels are denoted by the blue dotted line, while the best input parameter values are highlighted by the red line. The weight of BTE, NOx emissions, and MAPO are set equally. The model

predicts the most favourable settings for the input variables: SOI=-80 °CA, SEOI=-36.1 °CA, SIMP=15% and CA50=10.44 °CA (spark timing=-5.5°CA) to achieve the multiple objective optimizations.

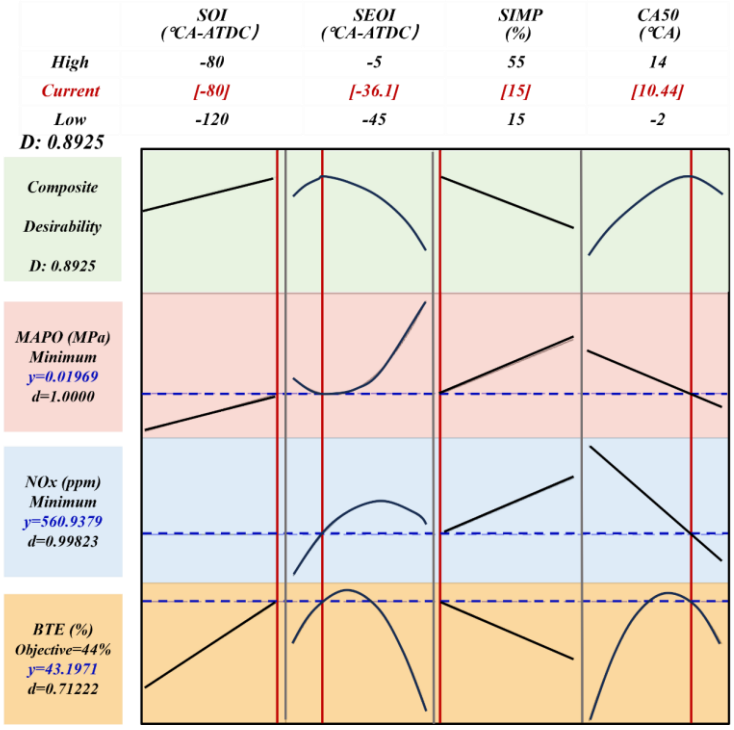


Fig. 18 Optimum factors and responses

The prediction results are shown in the left bar of Fig. 19. A BTE of 43.19%, NOx emissions of 560 ppm and MAPO of 0.019 MPa are estimated with a 95% confidence interval. The experiment is conducted based on the optimal settings and results are compared in detail. The test results illustrate the optimal condition can be achieved with a BTE of 43.03%, NOx emissions of 640 ppm and MAPO of 0.02 MPa. All experimental data points are located within the 95% confidence interval of the model predictions, proving the RSM model is accurate and reliable. After RSM optimization, the optimal split injection and ignition parameters are found to increase BTE with minimizing NOx emissions. The injection strategies differ from those proposed by Liang et al. [28]. In Liang's study, the optimal BTE is achieved with a SIMP of 40%, but NOx emissions increased by four times compared to a SIMP of 10%. The increase in SIMP shortened the

combustion duration (CA10-90), resulting in faster combustion and a sharp rise in combustion temperature, leading to a significant increase in NOx emissions. In contrast, this study identifies an optimal SIMP of 15%, which is similar to Feng et al. [47] studied on a GDI engine, where the optimal SIMP is 10%. The SEOI of -36.1°CA in this study allows only a short time for a small proportion of hydrogen to mix with air. The optimized split injection parameters create a stratification mixture near the spark plug with the appropriate concentration and a globally lean condition, as Han et al. [48] reported the effect of multiple injection on a GDI engine. Finally, by retarding the CA50 from 6°CA to 10.4°CA, a suitable flame propagation speed and combustion temperature are achieved, leading to increased BTE, reduced NOx emissions, and the avoidance of knock.

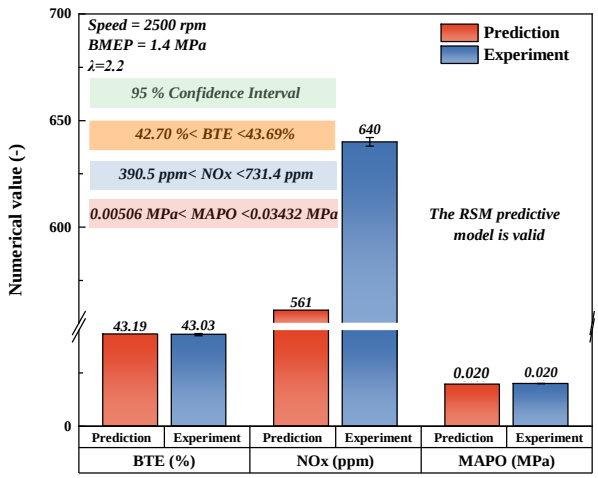


Fig. 19 Comparison between model prediction and experimental verification

Further injection and spark optimization is broadened to the whole operating map. As shown in Fig. 20, before optimization, the single injection SOI was consistently set at -140 °CA when the intake valve closed. Additionally, the BTE was found to exceed 38.9% under medium and high load conditions. However, the maximum BTE only reaches 40.51%. After the optimized single injection timing of SOI is set at -100 ° CA-ATDA (the orange point), the BTE is improved steadily with the injection optimization, especially at low

speed and partial load. For example, the most efficient BMEP decreases from 1.35 MPa to 1.08 MPa, while the BTE increases from 37.34 % to 40.19 % at 1500 rpm. At 2500 rpm, the maximum efficiency point of BMEP rises from 1.40 MPa to 1.55 MPa and, the BTE increases from 40.51 % to 42.53 %. In addition, when the optimized split injection (the purple point) is set as the SOI=-80 °CA-ATDA, SEOI=-36.1 °CA-ATDA, SIMP=15 %, the DI-H_2ICE can achieve the maximum BTE of 43.03%, which the BTE increased by 0.5% compared with the same working conditions at 2500 rpm before optimization. Meanwhile, the high efficiency region exceeds 40% with the medium and the high loads (BMEP from 0.72 MPa to 1.58 MPa), and the high BTE area is expanded by 30% compared to the load map of the original single injection strategy. The experimental research comparison of performance indicators such as BMEP, BTE, and NOx emissions is shown in Table. 8. Experimental data confirm that the split injection strategy enhances the power and efficiency of DI-H2ICE, effectively extending the operational range to include typical conditions for passenger and light-duty vehicles. This approach achieves high thermal efficiency, offering substantial practical value and potential for improved fuel economy in hydrogen energy vehicles.

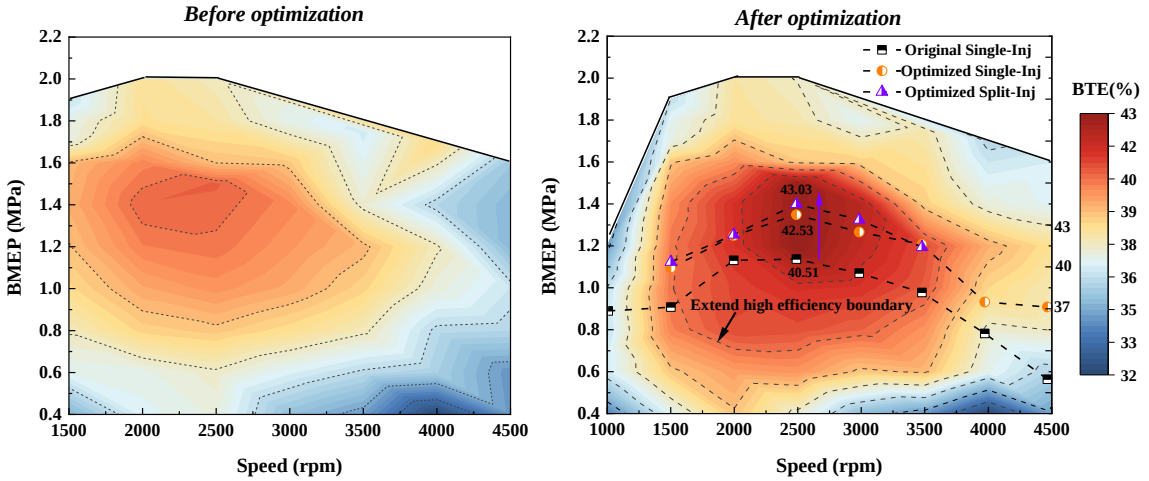


Fig. 20 Effect of optimized injection strategies on the DI-H_2ICE BTE.

Table. 8 The experimental research comparison of performance indicators

Main author	Speed	BMEP	BTE	NOx emissions	Injection strategies	Displacement

	rpm	MPa	%	ppm or g/kW·h	-	-
Present work	2500	1.40	43.03	640 ppm	DI, Split injection	4 Cylinders, 2.0 L
Bao et al.[13]	2000	1.76	42.06	>1400 ppm	DI, Single injection	4 Cylinders, 2.0 L
Luo et al.[49]	2000	<0.50	36.20	100 ppm	DI, Single injection	4 Cylinders, 1.5 L
Liang et al.[28]	1600	0.43	36.10	<0.1 g/kW·h	DI, Single injection	4 Cylinders, 2.0 L
Liang et al.[28]	1600	0.42	35.60	>0.4 g/kW·h	DI, Split injection	4 Cylinders, 2.0 L
Fu et al.[50]	1200	<0.3	33.46	6904 ppm	DI, Single injection	3 Cylinders, 1.5 L

4. Conclusion

In conclusion, this study presents significant advancements in the optimization of DI-H_2ICE through experimental and numerical investigations of injection strategies to achieve high thermal efficiency and low NOx emissions. The study leads to the following conclusions:

1) For single injection, inappropriate EOI=-47 °CA corresponding to SOI= -80 °CA causes discontinuous and non-uniform distribution of the mixture. Applying split injection strategies can avoid ultra-lean mixture distribution. Split injection forms a secondary swirl in the clockwise direction and reduces the total in-cylinder turbulent kinetic energy. Consequently, a continuous stratified mixture (λ=1.1~2) is formed near the spark plug, promoting the stable formation of flame kernels at the ignition timing. Moreover, it is necessary to take into account the synergistic influence of injection strategy, intake swirl, and combustion chamber configuration on mixture distribution and their impact on engine performance.

2) According to the experimental and numerical results, the near wall temperature of split injection is 217 K lower than that of single injection. The high-temperature region of split injection is more concentrated in the piston center, which reduces the heat transfer loss near the cylinder wall. As a result, split injection decreases the coolant energy proportion by 5.87 %, and increases the ITE and BTE from 47.68 % to 48.38 %,

and 41.74 % to 42.31 %, respectively. Therefore, optimizing the injection strategy can facilitate an in-cylinder mixture distribution that minimizes heat transfer losses. Additionally, an advanced cooling system can further enhance thermal efficiency when combined with optimized injection strategies.

3) The single-factor study of split injection parameters (SOI, SEOI and SIMP) and spark timing on the engine performance are obtained with different engine speeds. The optimal injection and spark timing is observed for each speed. The BTE of 2500 rpm is the highest among all engine speed conditions which exceeds 42% when the SOI=-100 °CA, SEOI= -25 °CA, SIMP=35% and CA50=6 °CA.

4) Multi-objective optimization was conducted based on the RSM method, with a CCD experiment designed to analyze the co-relationship of factors (split injection control parameters and CA50) on responses (BTE, NOx, and MAPO). Significant interaction effects are detected between the injection and spark. The results illustrate that the effects of SEOI and CA50 on BTE and NOx emission are more significant than SOI and SIMP, and the impact of CA50 on MAPO is more significant than others. The optimal parameters are predicted to be SOI=-80 °CA, SEOI=-36.1 °CA, SIMP=15%, and CA50=10.44 °CA at 2500 rpm.

5) Tests with these optimized parameters achieve a maximum BTE of 43.03% with low NOx emissions of 640 ppm, and MAPO of 0.02 MPa. Test results are located in the 95% confidence interval of the predicted values, confirming the accuracy of the RSM model. Further optimization of other engine speeds is developed. Before optimizing the injection strategy, the high thermal efficiency load range of DI-H_2ICE is only from BMEP 1.2 MPa to 1.57 MPa. After optimization, the high thermal efficiency range of DI-H_2ICE expanded from BMEP 0.72 MPa to 1.58 MPa, covering over 50% of the load map in the high thermal efficiency region.

5. Acknowledgements

This study was supported by the National Natural Science Foundation of China (Grant No.:52206228), the Natural Science Foundation of chongging Municipality (CSTB2023NSC0-MSX0399). This study was supported by the China Postdoctoral Science Foundation (2023M730238) and Young Elite Scientists Sponsorship Program by CAST (2023QNRC001). This study was supported by the Technology Integration Validation of Marine Low Carbon & Zero Carbon Low Speed Engine.

6. References

[1] The prospects for hydrogen as an energy carrier: an overview of hydrogen energy and hydrogen energy systems | Energy, Ecology and Environment n.d. https://link.springer.com/article/10.1007/s40974-016-0005-z (accessed March 25, 2024).

[2] Teoh YH, How HG, Le TD, Nguyen HT, Loo DL, Rashid T, et al. A review on production and implementation of hydrogen as a green fuel in internal combustion engines. Fuel 2023;333:126525. https://doi.org/10.1016/j.fuel.2022.126525.

[3] Escalante Soberanis MA, Fernandez AM. A review on the technical adaptations for internal combustion engines to operate with gas/hydrogen mixtures. International Journal of Hydrogen Energy 2010;35:12134–40. https://doi.org/10.1016/j.ijhydene.2009.09.070.

[4] Dimitriou P, Tsujimura T. A review of hydrogen as a compression ignition engine fuel. International Journal of Hydrogen Energy 2017;42:24470–86. https://doi.org/10.1016/j.ijhydene.2017.07.232.

[5] Shudo T. Improving thermal efficiency by reducing cooling losses in hydrogen combustion engines. International Journal of Hydrogen Energy 2007;32:4285–93. https://doi.org/10.1016/j.ijhydene.2007.06.002.

[6] Zhu S, Hu B, Akehurst S, Copeland C, Lewis A, Yuan H, et al. A review of water injection applied on the internal combustion engine. Energy Conversion and Management 2019;184:139–58. https://doi.org/10.1016/j.enconman.2019.01.042.

[7] Meng H, Ji C, Shen J, Yang J, Xin G, Chang K, et al. Analysis of combustion characteristics under cooled EGR in the hydrogen-fueled Wankel rotary engine. Energy 2023;263:125815. https://doi.org/10.1016/j.energy.2022.125815.

[8] Lai F, Sun B, Zhang Z, Zhang S, Wang K, Ju X, et al. Experimental investigation of the matching boundary and optimization strategy of a variable geometry turbocharged direct-injected

hydrogen engine. Fuel 2024;373:132288. https://doi.org/10.1016/j.fuel.2024.132288.

[9] Bao L, Sun B, Luo Q. Optimal control strategy of the turbocharged direct-injection hydrogen engine to achieve near-zero emissions with large power and high brake thermal efficiency. Fuel 2022;325:124913. https://doi.org/10.1016/j.fuel.2022.124913.

[10] Pandey JK, Dinesh MH, Kumar GN. A comparative study of NOx mitigating techniques EGR and spark delay on combustion and NOx emission of ammonia/hydrogen and hydrogen fuelled SI engine. Energy 2023;276:127611. https://doi.org/10.1016/j.energy.2023.127611.

[11] Koch DT, Sousa A, Bertram D, Koch DT, Sousa A, Bertram D. H2-Engine Operation with EGR Achieving High Power and High Efficiency Emission-Free Combustion, SAE International; 2019. https://doi.org/10.4271/2019-01-2178.

[12] Kawamura A, Sato Y, Naganuma K, Yamane K, Takagi Y. Development Project of a Multi-cylinder DISI Hydrogen ICE System for Heavy Duty Vehicles, 2010, p. 2010-01–2175. https://doi.org/10.4271/2010-01-2175.

[13] Bao L, Sun B, Luo Q, Li J, Qian D, Ma H, et al. Development of a turbocharged direct-injection hydrogen engine to achieve clean, efficient, and high-power performance. Fuel 2022;324:124713. https://doi.org/10.1016/j.fuel.2022.124713.

[14] Zhao F, Sun B, Yuan S, Bao L, Wei H, Luo Q. Experimental and modeling investigations to improve the performance of the near-zero NOx emissions direct-injection hydrogen engine by injection optimization. International Journal of Hydrogen Energy 2024;49:713–24. https://doi.org/10.1016/j.ijhydene.2023.09.039.

[15] Wei H, Hu Z, Ma J, Ma W, Yuan S, Hu Y, et al. Experimental study of thermal efficiency and NOx emission of turbocharged direct injection hydrogen engine based on a high injection pressure. International Journal of Hydrogen Energy 2023;48:12905–16. https://doi.org/10.1016/j.ijhydene.2022.12.031.

[16] Mohammadi A, Shioji M, Nakai Y, Ishikura W, Tabo E. Performance and combustion characteristics of a direct injection SI hydrogen engine. International Journal of Hydrogen Energy 2007;32:296–304. https://doi.org/10.1016/j.ijhydene.2006.06.005.

[17] Huang Z, Yuan S, Wei H, Zhong L, Hu Z, Liu Z, et al. Effects of hydrogen injection timing and injection pressure on mixture formation and combustion characteristics of a hydrogen direct injection engine. Fuel 2024;363:130966. https://doi.org/10.1016/j.fuel.2024.130966.

[18] Lee S, Kim G, Bae C. Effect of mixture formation mode on the combustion and emission characteristics in a hydrogen direct-injection engine under different load conditions. Applied Thermal Engineering 2022;209:118276. https://doi.org/10.1016/j.applthermaleng.2022.118276.

[19] Ye Y, Gao W, Li Y, Zhang P, Cao X. Numerical study of the effect of injection timing on the knock combustion in a direct-injection hydrogen engine. International Journal of Hydrogen Energy 2020:S0360319920326926. https://doi.org/10.1016/j.ijhydene.2020.07.117.

[20] Hu Z, Yuan S, Wei H, Huang Z, Wei H, Chan SH, et al. High-pressure injection or low-pressure injection for a direct injection hydrogen engine? International Journal of Hydrogen Energy 2024;59:383–9. https://doi.org/10.1016/j.ijhydene.2024.02.018.

[21] Kalaskar V, Conway G, Handa G, Joo S, Williams D, Kalaskar V, et al. Challenges and Opportunities with Direct-Injection Hydrogen Engines, SAE International; 2023. https://doi.org/10.4271/2023-01-0287.

[22] Hamzehloo A, Aleiferis P, Hamzehloo A, Aleiferis P. Numerical Modelling of Mixture

Formation and Combustion in DISI Hydrogen Engines with Various Injection Strategies, SAE International; 2014. https://doi.org/10.4271/2014-01-2577.

[23] Lee S, Kim G, Bae C. Effect of mixture formation mode on the combustion and emission characteristics in a hydrogen direct-injection engine under different load conditions. Applied Thermal Engineering 2022;209:118276. https://doi.org/10.1016/j.applthermaleng.2022.118276.

[24] Liang Z, Xie F, Jiang B, Li X, Su Y, Wang Z. Evaluating the potential of mixture formation methods to achieve efficient combustion and near-zero emissions on a hydrogen direct injection engine. Journal of Cleaner Production 2024;439:140930. https://doi.org/10.1016/j.jclepro.2024.140930.

[25] Wallner T, Scarcelli R, Nande AM, Naber J. Assessment of Multiple Injection Strategies in a Direct-Injection Hydrogen Research Engine. SAE Int J Engines 2009;2:1701–9. https://doi.org/10.4271/2009-01-1920.

[26] Yamane K. Hydrogen Fueled ICE, Successfully Overcoming Challenges through High Pressure Direct Injection Technologies: 40 Years of Japanese Hydrogen ICE Research and Development, 2018, p. 2018-01–1145. https://doi.org/10.4271/2018-01-1145.

[27] Welch A, Mumford D, Munshi S, Holbery J, Boyer B, Younkins M, et al. Challenges in Developing Hydrogen Direct Injection Technology for Internal Combustion Engines, 2008, p. 2008-01–2379. https://doi.org/10.4271/2008-01-2379.

[28] Liang Z, Xie F, Lai K, Chen H, Du J, Li X. Study of single and split injection strategies on combustion and emissions of hydrogen DISI engine. International Journal of Hydrogen Energy 2024;49:1087–99. https://doi.org/10.1016/j.ijhydene.2023.10.060.

[29] Li Y, Gao W, Zhang P, Ye Y, Wei Z. Effects study of injection strategies on hydrogen-air formation and performance of hydrogen direct injection internal combustion engine. International Journal of Hydrogen Energy 2019;44:26000–11. https://doi.org/10.1016/j.ijhydene.2019.08.055.

[30] Yosri M, Palulli R, Talei M, Mortimer J, Poursadegh F, Yang Y, et al. Numerical investigation of a large bore, direct injection, spark ignition, hydrogen-fuelled engine. International Journal of Hydrogen Energy 2023;48:17689–702. https://doi.org/10.1016/j.ijhydene.2023.01.228.

[31] Dayma G, Halter F, Dagaut P. New insights into the peculiar behavior of laminar burning velocities of hydrogen–air flames according to pressure and equivalence ratio. Combustion and Flame 2014;161:2235–41. https://doi.org/10.1016/j.combustflame.2014.02.009.

[32] Aung KT, Hassan MI, Faeth GM. Flame stretch interactions of laminar premixed hydrogen/air flames at normal temperature and pressure. Combustion and Flame 1997;109:1–24. https://doi.org/10.1016/S0010-2180(96)00151-4.

[33] Hu E, Huang Z, He J, Jin C, Zheng J. Experimental and numerical study on laminar burning characteristics of premixed methane–hydrogen–air flames. International Journal of Hydrogen Energy 2009;34:4876–88. https://doi.org/10.1016/j.ijhydene.2009.03.058.

[34] Kwon OC, Faeth GM. Flame/stretch interactions of premixed hydrogen-fueled flames: measurements and predictions. Combustion and Flame 2001;124:590–610. https://doi.org/10.1016/S0010-2180(00)00229-7.

[35] Grosseuvres R, Comandini A, Bentaib A, Chaumeix N. Combustion properties of H2/N2/O2/steam mixtures. Proceedings of the Combustion Institute 2019;37:1537–46. https://doi.org/10.1016/j.proci.2018.06.082.

[36] Kaczmarczyk KO, Liu X, Im HG, Turner JWG, Yuan H, Akehurst S, et al. Investigation of URANS CFD Methods for Supersonic Hydrogen Jets, Detroit, Michigan, United States: 2024, p. 2024-

01–2687. https://doi.org/10.4271/2024-01-2687.

[37] Wang K, Zhang Z, Sun B, Zhang S, Lai F, Ma N, et al. Experimental investigation of the working boundary limited by abnormal combustion and the combustion characteristics of a turbocharged direct injection hydrogen engine. Energy Conversion and Management 2024;299:117861. https://doi.org/10.1016/j.enconman.2023.117861.

[38] Fu Z, Gao W, Li Y, Hua X, Zou J, Li Y. Numerical simulation of the mixture distribution and its influence on the performance of a hydrogen direct injection engine under an ultra-lean mixture condition. International Journal of Hydrogen Energy 2023;48:19700–12. https://doi.org/10.1016/j.ijhydene.2023.02.041.

[39] Luo Y, Wu B, Li Q, Tang X, Yang Z, Wu C, et al. Experimental and simulation research on the lean combustion characteristics of direct-injection hydrogen engine. International Journal of Hydrogen Energy 2024;68:398–409. https://doi.org/10.1016/j.ijhydene.2024.04.184.

[40] Xu K, Liu Y, Zhao J, Zhang H, He X. Investigation of the dynamic interaction mechanism of split injections during the ignition process under diesel engine-like cold- and hot-start conditions. Fuel 2024;370:131830. https://doi.org/10.1016/j.fuel.2024.131830.

[41] Guan W, Gu J, Pan X, Pan M, Wang X, Zhao H, et al. Improvement of the light-load combustion control strategy for a heavy-duty diesel engine fueled with diesel/methonal by RSM-NSGA III. Energy 2024;297:131190. https://doi.org/10.1016/j.energy.2024.131190.

[42] Hamzehloo A, Aleiferis PG. LES and RANS modelling of under-expanded jets with application to gaseous fuel direct injection for advanced propulsion systems. International Journal of Heat and Fluid Flow 2019;76:309–34. https://doi.org/10.1016/j.ijheatfluidflow.2019.01.017.

[43] Luo Q, Sun B. Experiments on the effect of engine speed, load, equivalence ratio, spark timing and coolant temperature on the energy balance of a turbocharged hydrogen engine. Energy Conversion and Management 2018;162:1–12. https://doi.org/10.1016/j.enconman.2017.12.051.

[44] Szwaja S, Naber JD. Dual nature of hydrogen combustion knock. International Journal of Hydrogen Energy 2013;38:12489–96. https://doi.org/10.1016/j.ijhydene.2013.07.036.

[45] Ye Y, Gao W, Li Y, Zhang P, Cao X. Numerical study of the effect of injection timing on the knock combustion in a direct-injection hydrogen engine. International Journal of Hydrogen Energy 2020;45:27904–19. https://doi.org/10.1016/j.ijhydene.2020.07.117.

[46] Hong C, Ji C, Wang S, Xin G, Qiang Y, Yang J. Progressive strategies to avoid and exploit knock limit for optimal performance and stoichiometric operation of a DI hydrogen engine with high CR at WOT conditions. Fuel 2024;357:129849. https://doi.org/10.1016/j.fuel.2023.129849.

[47] Feng S, Hong W, Xie F, Yang Y, Su Y, Li X. Influence of stratified charge organized by double injection strategy on combustion and emissions on an EGR diluted GDI engine. Applied Thermal Engineering 2019;158:113803. https://doi.org/10.1016/j.applthermaleng.2019.113803.

[48] Han T, Singh R, Lavoie G, Wooldridge M, Boehman A. Multiple injection for improving knock, gaseous and particulate matter emissions in direct injection SI engines. Applied Energy 2020;262:114578. https://doi.org/10.1016/j.apenergy.2020.114578.

[49] Luo Y, Wu B, Li Q, Tang X, Yang Z, Wu C, et al. Experimental and simulation research on the lean combustion characteristics of direct-injection hydrogen engine. International Journal of Hydrogen Energy 2024;68:398–409. https://doi.org/10.1016/j.ijhydene.2024.04.184.

[50] Fu Z, Li Y, Wu W, Li Y, Gao W. Experimental study on the combustion and emission performance of the hydrogen direct injection engine. International Journal of Hydrogen Energy

2024;61:1047–59. https://doi.org/10.1016/j.ijhydene.2024.02.276.